THE JOURNAL OF PHYSICAL CHEMISTRY C

Article

Cite This: J. Phys. Chem. C 2019, 123, 13624−13636

pubs.acs.org/JPCC

Molecular Dynamics Simulations of the Adsorption of Phthalate Esters on Smectite Clay Surfaces

Jennifer A. R. Willemsen,*[,†] Satish C. B. Myneni,[‡] and Ian C. Bourg[†]

[†]Department of Civil & Environmental Engineering and [‡]Department of Geosciences, Princeton University, Princeton, New Jersey 08544, United States

Supporting Information

ABSTRACT: The partitioning of organic contaminants between water and solid surfaces is a key process controlling their fate and transport in natural environments. A novel methodology was developed to predict the adsorption of organic contaminants by smectite clay minerals (high specific surface area adsorbents abundant in natural soils) using molecular dynamics (MD) simulations. The methodology models a stack of flexible Ca-montmorillonite lamellae in direct contact with a bulk aqueous reservoir and uses the metadynamics technique to facilitate the exploration of the free energy landscape. The methodology was tested and validated in the case of six phthalate esters, widely used chemical plasticizers with endocrine disrupting properties. Simulation predictions reveal strong phthalate adsorption, especially for the larger and more hydrophobic phthalates. Predicted partition coefficients (K_d values) are consistent with collected batch experimental data. Adsorption was observed on both the exterior basal surfaces and within the interlayer nanopore, with phthalate molecules predominately adopting a flat orientation on the clay surface. Intercalation was also detected in complementary X-ray diffraction (XRD) experiments. A strong inverse relationship between extent of adsorption and clay surface charge density was observed, as phthalate molecules preferentially occupied the more hydrophobic uncharged patches on each surface. Detailed analysis of the free energy of adsorption revealed that phthalate affinity for the clay surface results from a small favorable van der Waals contribution and a large favorable entropic contribution. Overall, this research demonstrates the substantial affinity of smectite clays for phthalate esters and establishes a computational methodology capable of predicting the water−clay partition coefficients of organic contaminants, a key parameter in environmental fate and transport models.

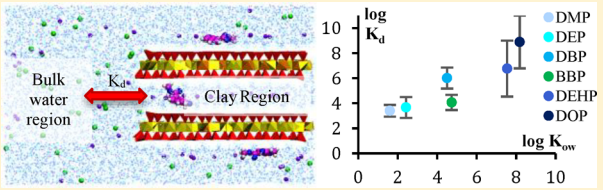

1. INTRODUCTION

The widespread distribution of organic contaminants in natural environments has posed a persistent and growing threat to human and ecosystem health for the past 50 years. Since the 1970s, the challenge has evolved from one of addressing a few classes of mostly nonpolar compounds (particularly polycyclic aromatic and chlorinated hydrocarbons) to a much more diverse range of substances (ranging from pharmaceuticals and plasticizers to pesticides, flame retardants, cosmetics, and recreational drugs) including many polar compounds. These newer, emerging contaminants are often present and harmful at low concentrations (ng L^{-1} to μg L^{-1}), and removal by wastewater treatment is costly and only partially effective.[1,2] The human health impacts of organic contaminant pollution are substantial, with the costs associated with endocrine disrupting compounds alone estimated at >$500 billion per year in the United States and Europe.[3−5] Mitigating the impacts of these contaminants remains one of the most important environmental issues of our time.

A key process controlling the fate and transport of nonvolatile organic contaminants is their tendency to partition between water and solid surfaces.[6,7] The main variable used to describe this tendency is the soil− or sediment−water partition coefficient (dm^3 kg^{-1}), which expresses the equilibrium concentrations of the organic contaminant in solution (C, mol dm^{-1}) and on solid surfaces (q, mol kg^{-1}) at trace levels of contaminant: $K_d = q/C$.[8,9] Attempts to predictively model this variable almost invariably rely on the knowledge that soil organic matter and clay minerals are the two predominant contributors to the specific surface area of soils and sediments and use the well-known component additivity approach, on which the overall adsorption coefficient is modeled as a weighted sum of adsorption coefficients on each solid phase:

$$K_d = f_{OC} K_{OC} + f_{clay} K_{clay} \quad (1)$$

In eq 1, f_{OC} and f_{clay} are the mass fractions of organic carbon and clay minerals in the dry soil and K_{OC} and K_{clay} are linear adsorption coefficients on the soil organic matter (normalized to organic carbon content) and clay fractions. In the case of nonpolar contaminants, K_d values in soils and sediments often correlate strongly with f_{OC}, suggesting that the last term in eq 1 can be neglected.[10−14] Whether this simplification can be extended to polar contaminants remains unclear: experimental evidence suggests that K_d values in soils are routinely larger

Received: February 26, 2019
Revised: May 10, 2019
Published: May 13, 2019

DOI: 10.1021/acs.jpcc.9b01864
J. Phys. Chem. C 2019, 123, 13624−13636

Table 1. Phthalate Structures, Molecular Weights and Volumes, Area Values, and log K_{ow} Values[75] [a]

Phthalate	Structure	Molecular Weight (g/mol)	Molecular Volume (Å^3)	Planar Molecular Area (Å^2)	Log K_{ow}
Dimethyl (DMP)	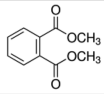	194.18	270.97	~90	1.60
Diethyl (DEP)	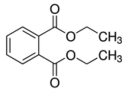	222.24	329.50	~110	2.42
Dibutyl (DBP)	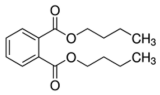	278.34	440.19	~147	4.50
Benzyl butyl (BBP)	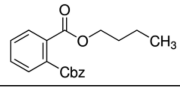	312.37	463.12	~154	4.73
Di(2-ethylhexyl) (DEHP)	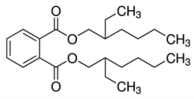	390.56	661.78	~221	7.54
Dioctyl (DOP)	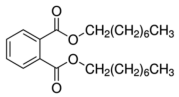	390.56	661.78	~221	8.18

[a]Molecular volume values were calculated by using reported phthalate densities. Planar molecular area values were estimated by dividing the molecular volume by the thickness of a planar phthalate molecule (~3 Å). Simulations (discussed below) confirmed the viability of the planar orientation.

than expected based on eq 1 with $K_{clay} \sim 0$, particularly in cases that involve clay rich soils or polar organic compounds.[15−20]

A recurrent theme in studies of mineral−organic interactions in soils and sediments is the potential role of smectites, a class of clay minerals abundant in temperate weathering environments.[21] These minerals have a high specific surface area (~780 m^2/g), a well-known hydrophobic character,[22,23] and the ability to accommodate (and potentially shelter) compounds in their interlayer nanopores.[24] Their affinity for organic compounds is much higher than that of most other soil minerals[25] and commensurate with that observed for organic carbon-rich soils.[26] Their potential importance is further suggested by extensive evidence that smectite abundance correlates with f_{OC} values in many soils and sediments.[27,28]

Despite extensive examination, however, the affinity of organic molecules for smectite surfaces remains poorly understood. For example, no consensus exists on the relative importance of different adsorption mechanisms such as hydrophobic or polar interactions.[25,29−34] One reason for the persistence of these unknowns is that clay charge density,[22,25] the type of isomorphic substitution,[34] the type of coordinating cation,[25,29,34] and the presence of other organic solutes[35] can each affect adsorption by several orders of magnitude. A second challenge is that smectite particles exhibit different types of surfaces (clay basal surfaces, edge surfaces, and interlayer nanopores) and that differences in smectite preparation, mineralogy, and aqueous chemistry can modulate adsorption by influencing the stacking and interlayer spacing of smectite particles.[36−38]

Molecular dynamics (MD) simulations have the potential to provide fundamental insight into smectite−organic interactions by probing adsorption on different regions of the clay surface in well-controlled conditions of particle aggregation and structural charge distribution. A key limitation of these simulations is that they probe short time scales (typically tens of nanoseconds) relative to the time required to sample adsorption and desorption of large organic molecules in different conformations on different parts of a clay particle with significant heterogeneity in topography and charge distribution. Because of this challenge, previous simulations have focused almost exclusively on characterizing stable configurations of organic molecules on clay surfaces (and their associated potential energies) rather than on quantifying the free energy of adsorption.[39−50] The few simulation studies that examined the adsorption free energy of organic molecules on smectite used simplified configurations with a single reaction coordinate, such as distance from an infinite clay basal surface or across the opening of a clay interlayer nanopore,[51,52] or did not allow for direct partitioning from a bulk aqueous region to the clay adsorption domains.[53] Overall, previous studies clearly demonstrate that organic contaminants have significant affinity for smectite basal surfaces and interlayer nanopores.[44,53] However, they have not yet given rise to a consistent picture of the magnitude or mechanisms of adsorption with different mechanisms including hydrophobic exclusion[52] and electrostatic and van der Waals (VdW) interactions[53] being proposed as drivers of adsorption.

To help overcome the challenges outlined above, we developed and tested a new MD simulation methodology for characterizing the adsorption of organic contaminants on smectite clay particles. Our methodology uses the metadynamics technique[54−57] and a recent extension of the CLAYFF interatomic potential model[58] to predict the partitioning of organic molecules between bulk-liquid-like water and a stack of flexible smectite particles with cleaved edges that offers multiple adsorption sites (external basal surface, edge surfaces, and interlayer nanopores) while allowing for feedbacks between adsorption and clay swelling and for complexity

DOI: 10.1021/acs.jpcc.9b01864
J. Phys. Chem. C 2019, 123, 13624−13636

arising from the random distribution of isomorphic substitutions in the clay particles.

To validate our new MD simulation methodology, we focused on the adsorption of the six phthalate esters that are present on the EPA priority pollutant list (Table 1). These phthalate esters constitute an ideal class of test compounds: they contain both polar and nonpolar moieties, are readily analyzed using fluorescence and UV spectroscopy, and are uncharged (hence their adsorption should be relatively insensitive to ionic strength). They span a wide range of octanol−water partition coefficients (log K_{ow} = 1.6−8.2) and molecular sizes, thus allowing an examination of the effects of hydrophobicity and steric constraints on adsorption. In addition, all six phthalates contain planar moieties (benzene ring and double-bonded ester oxygen) with the smaller phthalates (shorter alkyl chains) and benzylbutyl phthalate (extra benzene ring) having greater planar character. The ability of molecules to adopt a planar or near-planar orientation has important implications for the viability of intercalation into smectite interlayer regions. Finally, they are important environmental contaminants: they are widely used chemical plasticizers, pervasive in environmental waters and sediments, frequently detected at levels well above the EPA limit and WHO guideline,[59−62] and their metabolites are commonly found in human urine.[63] Exposure to phthalates has been linked to endocrine disrupting effects in rodents.[64−67] A relatively extensive database already exists on their adsorption in soils.[68−74] Our compilation of the existing database (Figure S1 in the case of DMP) shows no correlation between K_d and f_{OC} values, highlighting the need for new insight into their adsorption in soils and sediments.

2. METHODS

2.1. Molecular Dynamics Simulations. Molecular dynamics (MD) simulations were performed using a periodically replicated simulation cell (Figure 1) containing two

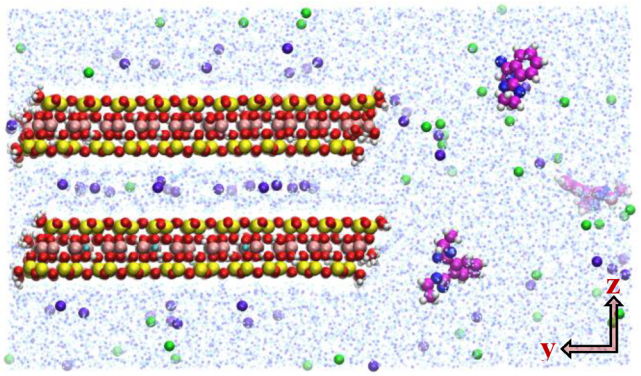

Figure 1. Simulation snapshot of two clay sheets in a system containing water molecules (small light blue spheres), calcium ions (purple spheres), chloride ions (green spheres), and phthalate molecules (magenta, dark blue, and white spheres).

lamellae of montmorillonite, the prototypical smectite clay mineral. Each lamella consisted of 60 montmorillonite unit cells and was 9.4 Å thick, 45.7 Å wide in the direction normal to the edge surfaces, and 63.36 Å long in the direction normal to the plane of the image in Figure 1 (essentially infinitely long because of the periodic boundary conditions). The simulations used the cis-vacant unit cell structure.[76] Clay edges were cleaved along the (110) and ($1\bar{1}0$) plane (the so-called AC edge) and healed by addition of O and H atoms to yield the expected structure and protonation state at near-neutral pH values.[77,78] Isomorphic substitutions of Al^{3+} by Mg^{2+} were randomly distributed within the octahedral layers of both clay lamellae including near the edge sites, with the stipulation that no two substitutions neighbor one another. This random distribution resulted in a small difference in surface charge density between the upper and lower clay lamellae (0.103 vs 0.094 C/m^2, respectively) that enabled examining the influence this parameter on phthalate adsorption, as discussed in more detail in the Results section. The negative structural charge of the clay lamellae was balanced by adsorbed Ca ions. The resulting unit cell formulas, $Ca_{0.275}Si_8Al_{3.45}Mg_{0.55}O_{20}(OH)_4$ and $Ca_{0.3}Si_8Al_{3.4}Mg_{0.6}O_{20}(OH)_4$ for the two clay lamellae, are characteristic of montmorillonite.[21] The two clay lamellae were stacked to form a particle with one interlayer nanopore and surrounded by liquid water (specifically, 6114 water molecules and 19.5 $CaCl_2$ ion pairs, resulting in a chloride concentration of 0.36 M). The initial interlayer nanopore size was set at 6 Å, representative of a two-water hydrate and in good agreement with reported interlayer hydration states for Ca-smectite.[79,80] Lastly, three identical phthalate molecules were added to the aqueous phase, far from the clay surfaces. Distinct simulations were performed with each of the six different phthalates examined in this study. After equilibration in the NP_yT ensemble, the simulation cell size was 63.36 Å × 81.04 Å × 46.80 Å for the system containing DMP and slightly larger in the y direction (by up to 0.31 Å) for simulations with larger phthalate molecules.

Interatomic interactions were described using the CLAYFF model for clay atoms,[81] the OPLS-AA model for phthalate molecules,[82] the SPC/E model for water molecules,[83] and well-established models for Ca and Cl.[84,85] This combination of force fields is known to accurately predict water structure and dynamics in bulk liquid water, in clay interlayer nanopores, and on external basal surfaces.[86−90] For clay−organic and silicate−organic systems, the selected force fields have been shown to accurately predict the interlayer structure and dynamics of organic molecules and the associated clay swelling,[91,92] but far fewer studies have experimentally validated the energetics of these systems.[44] The force fields used in this study all rely on fixed partial charges to describe Coulomb interactions and on the Lennard-Jones (LJ) 6−12 model to describe van der Waals (VdW) interactions. Lennard-Jones interaction parameters between unlike atoms were calculated using the Lorentz−Berthelot combining rules.

The CLAYFF model was initially developed to model infinite clay layers and does not specify interatomic interaction parameters for atoms on the clay edge surface. Most previous MD simulations of clay edges assumed that edge atoms have the same interatomic potential parameters as in the bulk clay structure.[51,93,94] However, about half of the edge O atoms are over- or undercoordinated from a bond-valence perspective and are therefore likely to have a different partial charge than fully coordinated CLAYFF O atoms.[78] Here, we used an approach developed by Lammers et al.[58] to derive CLAYFF-compatible partial charges for edge O atoms. Edge $-OH_2$ groups attached to Al atoms were modeled as water molecules as density functional theory (DFT) calculations indicate that these groups readily detach from the surface; the small partial charge difference between the previously defined $-OH_2$ groups and the newly defined water molecules was assigned

DOI: 10.1021/acs.jpcc.9b01864
J. Phys. Chem. C 2019, 123, 13624−13636

to the Al atom.[58] For consistency, the same approach was applied to edge $-OH_2$ groups attached to Mg atoms. The resulting clay edges carried no net proton surface charge. Throughout the course of our six >200 ns simulations, all edge hydroxyl groups remained attached and the structural integrity of the clay edges was preserved. Interatomic potential parameters used in our simulations are provided in the Supporting Information (Table S1).

Metadynamics simulations were performed using two reaction coordinates defined as the location of the center-of-mass of each phthalate molecule along the *y*- and *z*-axes of the simulation cell. During the metadynamics simulations, the effective free energy landscape explored by each phthalate molecule in the *yz*-plane was progressively modified through the addition, at regular time intervals δt, of a small positive bias potential (a Gaussian potential of height w and width σ_{ξ_i}) at the location of the phthalate molecule's center of mass. Simulations were run until all free energy minima were counteracted by the biasing potential and the phthalate molecules diffused randomly throughout the box (evaluation of this condition is nontrivial, as discussed below). The underlying free energy landscape was then determined as the inverse of the sum of biases added at any given position. As an alternative to the metadynamics technique, a 10 times larger and unbiased simulation of a system containing 30 DMP molecules was tested. However, this simulation showed insufficient adsorption−desorption events over the course of 100 ns to accurately determine a DMP water−clay partition coefficient.

A key feature influencing the accuracy of metadynamics simulations is the rate at which bias potential is added to the system. Slower addition of bias yields a more accurate free energy landscape at the expense of a longer simulation time, a particular issue since our landscape is larger than those typically explored using metadynamics.[57] If the bias is too large or added too frequently, however, "hill surfing", or the inaccurate buildup of bias in a given location, can occur.[56] Preliminary tests indicated that a relatively rapid addition of bias (δt = 1 ps, w = 5 meV, σ_{ξ_i} = 1.25 Å) allowed mapping the free energy landscape on time scales of ∼150 ns. However, such rapid addition of bias resulted in large temporal fluctuations in the free energy difference between the bulk water and clay regions. Our eventual methodology, therefore, used this relatively rapid addition of bias only during the initial part of the simulation (until all parts of the free energy landscape had been explored at least once by each of the three phthalate molecules, typically ∼100 ns). Then, the metadynamics simulation was continued using 30−45 ns of simulation with a 2 times smaller rate of bias addition (δt = 2 ps, w = 5 meV, σ_{ξ_i} = 1.25 Å) followed by 100 ns of simulation with a 4 times smaller rate of bias addition (δt = 2 ps, w = 2.5 meV, σ_{ξ_i} = 1.25 Å). This simulation methodology provided a reasonable balance between simulation time and accuracy as quantified by comparing the free energy maps independently determined for each of the three phthalate molecules in the simulation cell.

Simulations were run on the Cori supercomputer at the National Energy Research Scientific Computing Center (NERSC) using the LAMMPS program[95] with the LAMMPS colvars package.[96] Each system was equilibrated for a total of 445 ps (including 200 ps of equilibration in the NP_yT ensemble at P_y = 1.0 bar) and then simulated for up to 350 ns in the NVT ensemble by using the metadynamics technique. All simulations were performed at 298 K with a time step of 1 fs. Newton's equations of motion were solved using the Verlet algorithm. Short-range LJ and Coulomb interactions were solved up to 12 Å. Long-range Coulomb interactions beyond 12 Å were solved in k-space using the particle−particle/particle-mesh (PPPM) method[97] with an accuracy of 99.9%. The SHAKE algorithm[98] was used to keep water molecules rigid. One of the clay layers was held in place by resetting its overall translational and rotational velocity (excluding hydrogen atoms) to zero at each time step. The second clay layer was similarly constrained with regard to rotation and translation in the *xy*-plane but was allowed to translate in the *z*-direction (to enable clay swelling).

2.2. Analysis of Simulation Results. Simulation output was analyzed using in-house Matlab scripts and visualized in VMD.[99] Analysis of the adsorption energetics relied on two-dimensional maps of the free energy landscape reported for each phthalate molecule every 5 ns and temporally averaged over the course of the last 100 ns of simulation. A bulk liquid water region was defined as the 10 Å × 46.8 Å water region located at least 10 Å from the clay edges, and a clay region was defined as the middle 30 Å × 46.8 Å region of the clay sheet, leaving an ∼10 Å buffer on either side to avoid edge effects. The predicted free energy of transferring a phthalate molecule from the bulk water region to the clay region, $\Delta F_{water\rightarrow clay}$, was calculated by averaging the metadynamics predictions of the local free energies $\Delta F(y,z)$ in each region in a manner consistent with statistical thermodynamics:

$$\Delta F_{water\rightarrow clay} = -RT \ln\langle e^{-\Delta F/RT}\rangle_{clay} + RT \ln\langle e^{-\Delta F/RT}\rangle_{water} \quad (2)$$

where R is the ideal gas constant, T is absolute temperature, and $\langle\ \rangle_i$ denotes a spatial average in region i. Free energies obtained via eq 2 express the expected ratio of the average number of moles of phthalate in the bulk water region (n_{water}) and in the clay region (n_{clay}) in an unbiased simulation:

$$\frac{n_{clay}/V_{clay}}{n_{water}/V_{water}} = e^{-\Delta F_{water\rightarrow clay}/RT} \quad (3)$$

where V_{water} and V_{clay} are the volumes of the bulk water and clay regions. The total number of moles in the clay region (n_{clay}) can be expressed as the sum of an adsorbed term (n_{ads}) and a nonadsorbed aqueous term (n_{free}):

$$n_{ads} = q_{clay} M_{clay} \quad (4)$$

$$n_{free} = C_{water} V_{clay} \frac{\rho_{H_2O\_clay}}{\rho_{H_2O\_water}} \quad (5)$$

where q_{clay} (mol kg_{clay}^{-1}) is the adsorbed phthalate concentration, M_{clay} is the mass of clay within the clay region, C_{water} is the bulk aqueous concentration, and $\rho_{H_2O\_clay}$ and $\rho_{H_2O\_water}$ are the average molecular densities of water (mol L^{-1}) in the clay and bulk water regions, respectively. The inclusion of the nonadsorbed aqueous term makes the overall calculation consistent with Gibbs' definition of adsorption as a surface excess.[100] The total number of moles in the bulk water region can be expressed as

$$n_{water} = C_{water} V_{water} \quad (6)$$

DOI: 10.1021/acs.jpcc.9b01864
J. Phys. Chem. C 2019, 123, 13624−13636

Finally, eqs 3−6 can be combined with the definition of K_d to obtain an expression for K_d as a function of the free energy difference $\Delta F_{water\rightarrow clay}$ predicted by using metadynamics:

$$K_d = \frac{q_{clay}}{C_{water}} = \frac{V_{clay}}{M_{clay}}\left[e^{-\Delta F_{water\rightarrow clay}/RT} - \frac{\rho_{H_2O\_clay}}{\rho_{H_2O\_water}}\right] \quad (7)$$

We note, in passing, that a strictly equivalent expression for K_d could have been obtained by excluding the volume of the inaccessible solid phase both from the definition of the clay region and from the calculation of the average free energy within this region. The expression derived above, however, has the advantage of requiring no independent knowledge of the location of the water−clay interface.

Metadynamics was performed independently for each phthalate molecule. Adsorption free energies calculated with each molecule were considered as separate replicates allowing for the calculation of statistical error. Our simulation predictions were performed at constant volume, such that the resulting calculations yield predictions of the Helmholtz free energy and constant-volume K_d values. However, since the simulations were initially equilibrated in the NP_yT ensemble at P_y = 1 bar, the pressure−volume term relating the Helmholtz free energy to the Gibbs free energy should be negligible, enabling comparison with our experimental results (section 3.3).

A set of shorter simulations was conducted without metadynamics to examine the configuration and energetics of adsorbed phthalate molecules. For these simulations, the system was initially equilibrated for 5 ns with phthalate molecules close to three different adsorption domains (upper basal surface, lower basal surface, and interlayer region) followed by a 25 ns production run. Results of these unbiased simulations were examined to determine the average density distributions of adsorbed phthalate molecules in directions parallel to the clay surface (relative to the location of isomorphic substitutions and exchangeable Ca ions) and normal to the clay surface as well as the average potential energy (E_{pot}) contributed by pairwise VdW and Coulomb interactions between the phthalate molecules and other atoms in the simulated systems.

2.3. Batch Adsorption and X-ray Diffraction Experiments. Experimental data were collected for a subset of the phthalate esters to validate our MD simulations. Dimethyl phthalate, diethyl phthalate, dibutyl phthalate, calcium chloride dihydrate, sodium acetate, and acetic acid were purchased from Sigma-Aldrich. All chemicals were analytical grade. Reference montmorillonite (SWy-3) was obtained from the Clay Minerals Society Source Clays Repository. Prior to use, the clay was purified using a protocol derived from previous studies.[101,102] Briefly, the clay was dispersed in ultrapure water, and coarse impurities (>2 μm) were removed by particle size fractionation using low-speed centrifugation. The clay was then washed three times with 1 M sodium acetate/acetic acid buffer to remove carbonate impurities followed by three washes with 1 M $CaCl_2$ to homoionize the samples. Finally, excess salts were removed by dialysis (120 h) and dried on a lyophilizer. Analysis of the purified clay by X-ray diffraction (XRD) at ambient relative humidity indicated the absence of crystalline impurities and a basal spacing of 15.56 Å characteristic of the two-layer hydrate of montmorillonite.[103]

Standard batch adsorption experiments were performed in triplicate to determine partition coefficients for DMP and DEP. A detailed procedure is described in the Supporting Information. Plots of adsorbed concentration q vs solution concentration C yielded linear isotherms for the full concentration range examined experimentally (C = 5−80 μM for DMP and C = 0.5−20 μM for DEP) and K_d values where determined by linear regression of the experimental data on q vs C.

Phthalate-loaded clay slurries were dried on glass slides and analyzed using XRD to search for evidence of clay interlayer expansion associated with DMP, DEP, and DBP adsorption. Samples were analyzed at ambient humidity and temperature using a high-resolution Bruker D8 Discover X-ray diffractometer with a copper X-ray source and a corresponding incident X-ray wavelength of λ = 1.5406 Å using a scan speed of 0.5° 2θ/min and a step size of 0.02° 2θ.

3. RESULTS AND DISCUSSION

3.1. Metadynamics Prediction of the Free Energy Landscape. Metadynamics reconstructions of the free energy landscape explored by phthalate molecules are shown in Figure 2A for the six phthalates examined in this study. As expected, free energy is spatially uniform in the bulk aqueous region. Free energy minima are evident both on the external basal surfaces of the clay stack and within the interlayer nanopore. Little or no affinity is seen for the clay edge surfaces.

Free energy profiles as a function of y and z were obtained by averaging the results in Figure 2A along the z-coordinates (Figure 2B) and clay region y-coordinates (Figure 2C), respectively. The results shown in Figure 2 clearly demonstrate the similarity between the locations of the free energy minima for the six phthalates, suggesting the presence of preferential adsorption domains on the clay surface.

3.2. Predicted Partition Coefficients. Predicted water−clay partition coefficients (i.e., K_d values) are shown in Table 2 as calculated via eqs 2−7 for the system as a whole and for subsets of the clay surface (i.e., upper and lower exterior basal surfaces, interlayer nanopore). Standard deviations were calculated by comparing the temporal averages of the free energies of adsorption of the three phthalate molecules in each simulation. For all phthalates, adsorption was significantly greater on the less charged lower external basal surface (0.094 C/m^2) relative to the upper external basal surface (0.103 C/m^2), suggesting that the K_d values of phthalates on smectite are highly sensitive to surface charge density. This stronger adsorption of uncharged organic solutes on lower charge smectites is consistent with previous experimental observations.[25]

In addition to the strong influence of surface charge density, the metadynamics predictions of K_d show a strong influence of the size of the phthalate molecule: the overall K_d value increases by 5.4 orders of magnitude when going from the smallest (DMP) to the largest (DOP) phthalate. This trend is consistent with the expected increase in adsorption with greater hydrophobicity and lower solubility.[16] On the upper clay sheet and in the interlayer region, the trend with solute size is less clear. Intercalation is predicted to be favorable for all phthalates except DEHP, the bulkiest of the phthalates in this study, likely due to steric hindrance and a possible entropic penalty for this branched molecule to adopt the necessary planar conformation for interlayer adsorption.

3.3. Experimental Validation. Batch adsorption experiments performed with DMP and DEP yielded linear isotherms (Figure S2). As predicted using metadynamics, adsorption

DOI: 10.1021/acs.jpcc.9b01864
J. Phys. Chem. C 2019, 123, 13624−13636

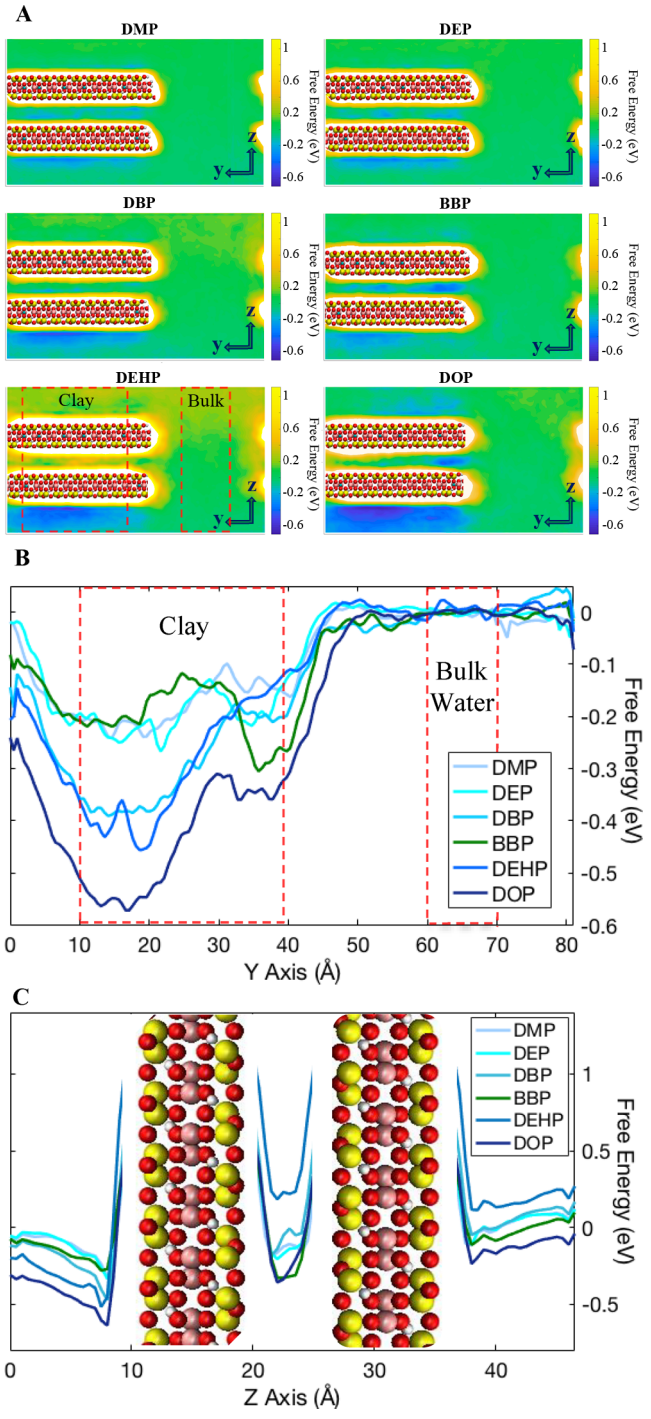

Figure 2. (A) Two-dimensional free energy maps (in the *yz*-plane) for DMP, DEP, DBP, BBP, DEHP, and DOP predicted using metadynamics. Each map is the average calculated for the three molecules in the system. The bulk region is normalized to zero. Bright yellow regions reflect VdW repulsion in the close vicinity of the clay sheets. Blue regions correspond to free energy wells. Red dashed boxes indicate the defined clay and bulk water regions used in eq 2. (B, C) One-dimensional free energy profiles as a function of *y* (B) and *z* (C) for the six phthalates calculated from the data in (A). Light to dark blue lines show results obtained for phthalates with increasing numbers of alkyl C atoms; the green line shows the result obtained for the phthalate with a benzyl group. The steep energetic increase near the clay surface in (C) is due to strong short-range VdW repulsion.

increased with the size of the phthalate molecule. Linear regression of the adsorption results yields log K_d values of 1.8 ± 0.1 and 2.3 ± 0.1 for DMP and DEP, respectively. The measured partition coefficients are of similar magnitude to those reported for other neutral polar organic compounds,[26] but the DEP K_d value is 1.4 ± 0.1 orders of magnitude larger than that previously reported by Wu et al.[104] in conditions analogous to our experiments. The reason for this difference is unclear but may reflect the high sensitivity of adsorption to surface charge density noted above.

Comparison between our predicted and measured log K_d values for DMP and DEP (Table 2) provides a partial validation of our simulation methodology. Measured values were consistently within the range of K_d values predicted for the three different regions of the clay surface. Perhaps more significantly, measured K_d values were closest to the predicted K_d values in the interlayer nanopores, in agreement with the expectation that most of the basal surface area in our experiments is likely located in such nanopores (experimental studies indicate that Ca-montmorillonite lamellae in dilute aqueous suspensions form stacks of 3−20 layers).[38]

As noted in the Methods section, a subset of the phthalate-loaded clay slurries was examined using XRD at ambient relative humidity to search for evidence of phthalate intercalation in clay interlayer nanopores. Results regarding the position of the d_{001} peak are presented in Table S2, and representative XRD spectra are shown in Figure S3. Briefly, experiments performed at low loadings (specifically, experiments that used 100 μM solutions or less) yielded no evidence of interlayer expansion, while experiments that probed higher loadings (1000 μM solutions) showed a clear increase in interlayer spacing from 15.4 ± 0.1 Å (characteristic of a two-water calcium hydrate at ambient relative humidity) to 16.0 Å for DMP, 17.3 Å for DEP, and 16.6 Å for DBP.

3.4. Phthalate Density Distribution on the Clay Basal Surfaces. To gain further insight into the charge dependence of phthalate adsorption, we calculated the average density distribution of phthalate molecules on the upper and lower siloxane surfaces and in the interlayer nanopore in our unbiased simulations (i.e., without metadynamics). More precisely, we calculated maps of average phthalate and calcium density in the *xy*-plane within ∼4.5 Å of the clay siloxane surface oxygen atoms in the three adsorption regions (interlayer, bottom, and top). The resulting phthalate density maps are shown on the left side of Figure 3 in the case of DMP, superimposed on the location of isomorphic substitutions in the nearby clay lamella(e). The right side of Figure 3 shows the locations of Ca ions in the three regions during the same simulation (recorded every 1 ps for 5 ns) as well as a representative snapshot of the DMP molecule in the highest affinity patch in each region.

As shown in Figure 3, a strong relationship is observed between regions of high phthalate density and regions devoid of isomorphic substitutions. In particular, the largest uncharged patch (diameter ∼ 23.5 Å), located on the lower external basal surface, was the location with the highest phthalate density for all six phthalate molecules. The location of this large uncharged patch is consistent with the location of the deepest free energy well for all compounds except BBP in Figure 2. On the upper external basal surface, the largest uncharged patch (diameter ∼ 16.5 Å) is considerably smaller, corroborating the differences in adsorption selectivity. The lack of a particularly favorable adsorption site on the upper surface is further

DOI: 10.1021/acs.jpcc.9b01864
J. Phys. Chem. C 2019, 123, 13624−13636

Table 2. Phthalate log K_d Values ($dm^3\ kg^{-1}$) Predicted by Using Metadynamics (Either for the Overall System or on Different Parts of the Clay Surface) or Measured Using Batch Adsorption Experiments[a]

	predicted log K_d				
phthalate	overall	interlayer nanopore	lower surface	upper surface	measured log K_d
DMP	3.4 ± 0.5	1.8 ± 0.9	4.0 ± 0.3	0.6 ± 0.1	1.8 ± 0.1
DEP	3.7 ± 0.8	2.0 ± 0.6	4.3 ± 0.9	0.4 ± 0.2	2.3 ± 0.1
DBP	6.0 ± 0.8	1.4 ± 0.3	6.6 ± 0.8	–	*NA*
BBP	4.1 ± 0.6	4.3 ± 0.6	3.6 ± 0.9	0.8 ± 0.9	*NA*
DEHP	6.8 ± 2.2	–	7.4 ± 2.2	–	*NA*
DOP	8.9 ± 2.1	4.5 ± 0.6	9.5 ± 2.2	2.7 ± 1.3	*NA*

[a]For the predicted values, dashes indicate regions where adsorption was unfavorable. Reported error estimates are 95% confidence intervals.

evidenced by the larger area explored by the phthalate molecule on this surface.

The results shown in Figure 3 are consistent with previous studies indicating that the adsorption of other uncharged organic contaminants (atrazine and nitroaromatics) on smectite correlates inversely with surface charge density[25,105] and partly corroborates previous suggestions that adsorbed Ca^{2+} ions inhibit the adsorption of uncharged organic contaminants.[25,41] The charge density of SWy-3 montmorillonite used in our experimental study has been reported to be on the order of 0.096 C/m^2,[106] between the calculated values of 0.094 and 0.103 C/m^2 for the lower and upper clay lamellae in our simulations. Given the observed sensitivity of phthalate adsorption to clay charge density and the typical accuracy of experimental measurements of smectite surface charge density (on the order of 5−10% relative error),[107−110] these charge density values are consistent with our measured log K_d values falling roughly between the values predicted for the upper and lower surfaces in our simulations.

3.5. Conformation of Adsorbed Phthalates. Density profiles of water oxygen, calcium, and phthalate atoms as a function of distance normal to the clay basal surfaces are shown in Figure 4 (left). The sharp peaks ∼4 Å from the clay surface O atoms for DMP, DEP, DBP, and BBP indicate that these molecules predominantly form inner-sphere surface complexes that lie flat on the clay basal surface while adopting a predominately planar conformation. In the case of DEHP and DOP, the aromatic ring and ester groups also tend to lie flat on the surface, while the bulkier side chains extend farther from the surface resulting in broader peaks. Inner-sphere surface complex formation is further confirmed by the displacement of water molecules in the first water layer coordinating the clay sheet (Figure S4). Analysis of the locations of individual atom types within the phthalate molecules (shown in the right panel of Figure 4 in the case of DMP) reveals that the aromatic and ester carbon atoms (C1 and C2) tend to lie in a plane on the siloxane surface with their aromatic H atoms (H1) slightly tilted toward the surface. The two ester oxygens (O1 and O2) and the methyl group at the end of the ester chains (C3), however, alternate between lying on the clay surface and pointing away from the surface, particularly in the case of the highly polar ester C═O oxygen (O1). This overall orientation parallel to the clay surface is consistent with hydrophobic adsorption (it minimizes phthalate contact with water molecules) and agrees with experimental spectroscopic studies of aromatic organic compound adsorption.[41] The tendency of the ester C═O oxygen to point away from the surface about half the time is consistent with its high negative partial charge (−0.43*e*), resulting in significant affinity for water.

Within the interlayer region, two molecular orientations were commonly observed. For the smaller phthalate molecules, both visual observation and the density profiles indicate a predominately flat orientation, especially on the lower clay sheet. However, the molecules occasionally adopt a bridging orientation (shown in the center panel of Figure 4) in which they simultaneously interact with both siloxane surfaces. For the larger phthalate molecules (DEHP and DOP), the bridging orientation was the most common interlayer configuration, perhaps reflecting the absence of large calcium-free patches.

3.6. Potential Energy of Free and Adsorbed Phthalates. Analysis of the pairwise interaction energies between phthalate atoms and all other atoms in our simulations enabled calculating the average potential energy (E_{pot}) of a phthalate molecule in bulk liquid water and on the three regions of the clay surface defined above. Potential energies were determined by using unbiased simulation trajectories for the adsorbed phthalates and metadynamics simulation trajectories for the nonadsorbed phthalates. Decomposition into phthalate interactions with different neighbors showed that phthalate−clay and phthalate−water interactions account for more than 96% of the reported interactions when the phthalate is adsorbed, with minimal contributions from phthalate−phthalate or phthalate−ion interactions (<0.1% and <3%, respectively). Decomposition of phthalate potential energy into van der Waals (VdW) and Coulomb contributions is presented in Figure 5.

As shown in Figure 5, Coulomb interactions show little variability with phthalate type. This observation is consistent with the fact that all phthalates contain one aromatic and two ester groups and polar interactions involving these groups dominate the Coulomb contribution. The only (minor) outlier to this trend is BBP, which consistently forms slightly stronger Coulomb interactions as a result of having an extra aromatic ring. Coulomb interactions are essentially identical in bulk liquid water and in the three clay surface regions, indicating that these interactions contribute very little to adsorption (<0.1 eV).

Conversely, VdW interactions increase significantly with the size of the phthalate molecule, as expected since each additional C atom contributes almost equally to VdW interactions on the OPLS-AA model used in our simulations. Furthermore, VdW interactions are systematically more favorable on the clay surface than in bulk liquid water by a factor of 0.1−0.2 eV. Overall, VdW interactions account for most of the difference in potential energy observed between the bulk water region and adsorption domains.

3.7. Enthalpic and Entropic Effects. The results shown in Figure 5 can be readily expressed as a difference in potential energy between each phthalate in bulk liquid water and in each

DOI: 10.1021/acs.jpcc.9b01864
J. Phys. Chem. C 2019, 123, 13624−13636

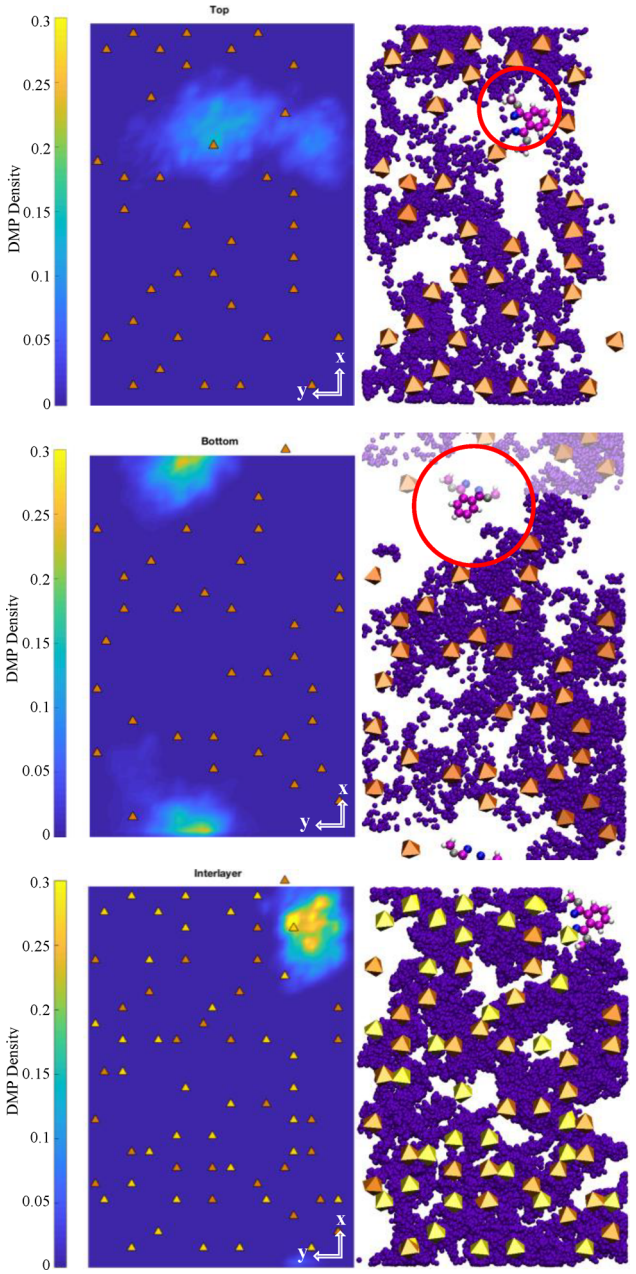

Figure 3. Left: average DMP density in the *xy*-plane (parallel to the clay surface) in the three regions located within ~4.5 Å of the surface O atoms (upper and lower external basal surfaces and interlayer nanopore) for 5 ns of unbiased MD simulation. Right: location of Ca ions in the same regions recorded every 1 ps during the same simulation (purple spheres) along with the location of isomorphic substitutions in the nearby clay lamella(e) (orange and yellow octahedra) and a representative snapshot of the location of the adsorbed DMP molecule. The red circles highlight the largest uncharged patches on the upper and lower basal surfaces.

adsorption domain. If we neglect the small differences in intramolecular interactions between free and adsorbed phthalates, this difference in potential energy closely approximates the enthalpy of adsorption ΔH_{ads}. Predictions of this enthalpy of adsorption on the upper and lower external basal surface and in the interlayer region are shown as red diamonds in Figure 6. Enthalpic interactions have a small favorable impact on phthalate adsorption in all three regions but do not contribute to the large selectivity difference between the three regions. The overall enthalpies of adsorption predicted by our simulations range from −0.10 to −0.04 eV, in good agreement with the experimental results reported by Wu et al.[104] at low phthalate loadings.

In Figure 6, we also report the difference between the free energy of adsorption and the enthalpy of adsorption ΔH_{ads}. For comparison with our predicted values of ΔH_{ads}, we calculated the free energy of adsorption $\Delta F_{ads} = -RT \ln(K_d \times M_{clay}/V_{water\_in\_clay} + 1)$, where $V_{water\_in\_clay}$ represents the volume of water in the clay region and K_d was calculated via eq 7. The definition of ΔF_{ads} (free energy of partitioning into the water within the clay region) is closely related to that of $\Delta F_{water \rightarrow clay}$ (free energy of partitioning into the clay region) but enables a more direct comparison with our calculated values of the enthalpy of adsorption. If we neglect the small pressure−volume term that relates the Gibbs and Helmholtz free energies of adsorption, the difference between ΔF_{ads} and ΔH_{ads} equals the entropic contribution to adsorption ($-T\Delta S_{ads}$). As shown in Figure 6, our results highlight the importance of entropy as the main driving force behind phthalate adsorption, particularly on the high-affinity lower external basal surface (i.e., the region with relatively large uncharged patches). For the bottom clay sheet, the entropic contribution to adsorption scales linearly with planar molecular area (R^2 = 0.59); the inverse slope of this regression (30.7 ± 6.3 mN/m) has units of interfacial energy and a magnitude commensurate to that of the water−air interface predicted by the SPC/E water model (61.3 mN/m at 300 K).[111] With the exception of DOP, entropic interactions are unfavorable on the upper, more charged external basal surface. This likely reflects the absence of large hydrophobic adsorption domains on this surface from which water can be favorably removed to accommodate phthalate adsorption.

On the basis of the strong correlation between phthalate adsorption and surface charge density evidenced above, one might expect adsorption to be weakest in the interlayers relative to both external surfaces. As shown in Figure 6, however, predicted free energies and entropies of adsorption in the interlayers fall between those on the upper and lower external surfaces for DMP, DEP, DBP, and DOP. For BBP, adsorption is equally favorable in the interlayer and on the lower basal surface. The only exception is for DEHP, the bulkiest and therefore most sterically hindered of the phthalate molecules examined here. This finding suggests that although the interlayer nanopores inherently contain fewer, smaller regions with no nearby surface charge, those uncharged patches that do exist in the interlayers are inherently more hydrophobic than on external basal surfaces, perhaps because they contain water that is inherently less bulk-liquid-like.[78,112] This hypothesis is consistent with the strong localization of interlayer phthalate density in Figure 3 and, also, with the ability of adsorbed phthalate molecules to adopt a tilted configuration in the interlayer.

4. CONCLUSIONS

The clay−water partition coefficients predicted in this study are commensurate with reported K_{oc} values for phthalate partitioning to organic carbon in natural soil systems.[68−74] The predicted partition coefficients, furthermore, exhibit a strong correlation with K_{ow} similar to trends relating K_{oc} and K_{ow} for various hydrophobic chemicals (Figure 7).[13,14,113−129] These results reinforce previous evidence that smectite clay minerals have a strong affinity for certain organic contaminants. Our

DOI: 10.1021/acs.jpcc.9b01864
J. Phys. Chem. C 2019, 123, 13624−13636

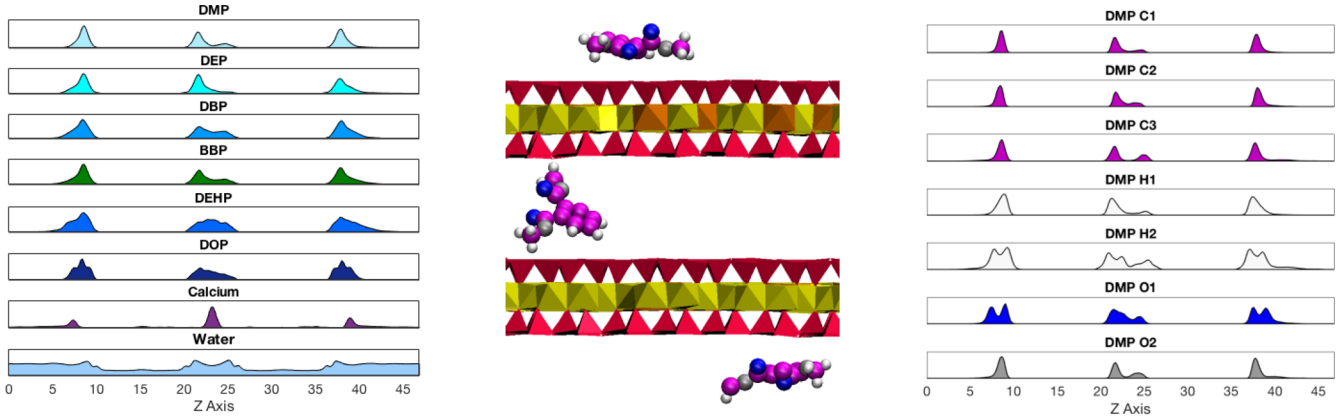

Figure 4. Left: density profiles for the six phthalate esters, water, and calcium along the *z*-axis of the simulation box. Center: snapshot of the three DMP molecules in the unbiased simulation showing molecules lying flat on the exterior surfaces and adopting a bridging configuration in the interlayer. Carbon atoms are depicted in magenta, hydrogen in white, the ester C═O oxygen in blue, and the second ester oxygen in silver. Clay SiO_4 tetrahedra are in red, AlO_6 octahedra in yellow, and MgO_6 octahedra in orange. Right: density profiles for the individual atom types in DMP. C1 represents aromatic carbons, C2 is the ester carbon, and C3 is the tail methyl carbon. H1 and H2 are the aromatic and methyl hydrogen atoms, respectively. O1 is the ester C═O, and O2 is the second ester oxygen atom.

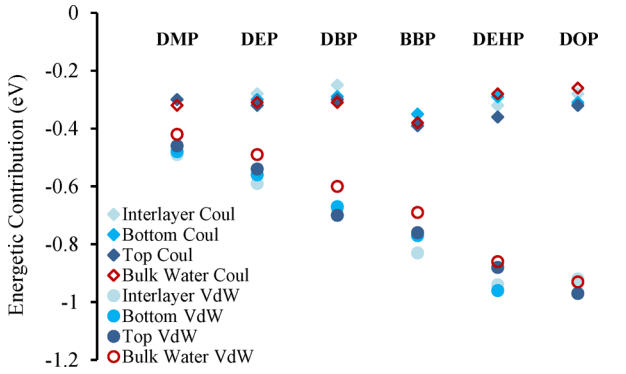

Figure 5. Coulomb (diamonds) and VdW (circles) contributions to the average potential energy of a phthalate molecule in bulk liquid water, in the interlayer nanopore, and on the upper or lower external basal surfaces. The 95% confidence intervals range from <0.01 to 0.04 eV. Full results are shown in Table S3.

finding that this affinity is strongly localized in hydrophobic patches on the clay basal surface suggests that contaminant adsorption may be readily inhibited by organic carbon in a natural system. The interplay between water, organic-carbon-coated-clay, and organic contaminants may be a fruitful area of future research.

The results presented above also have potential implications with regard to the importance of smectite clay minerals in the microbial degradation of soil organic matter (SOM). Briefly, the phthalate esters examined here likely approximate certain properties of SOM as their stoichiometry and size falls within the ranges reported for dissolved and mineral-associated fractions of SOM. The results obtained in this study support previous research suggesting strong adsorption of aromatic SOM by minerals.[130,131] However, the energetic results presented here highlight the dominant role of entropy as a driver of adsorption, contrary to the belief that SOM adsorption is driven by specific interactions between polar functional groups and mineral surfaces.[130−132] Exploration of the adsorption of a broader range of compounds representative of SOM may help shed additional light on the relevant interactions.

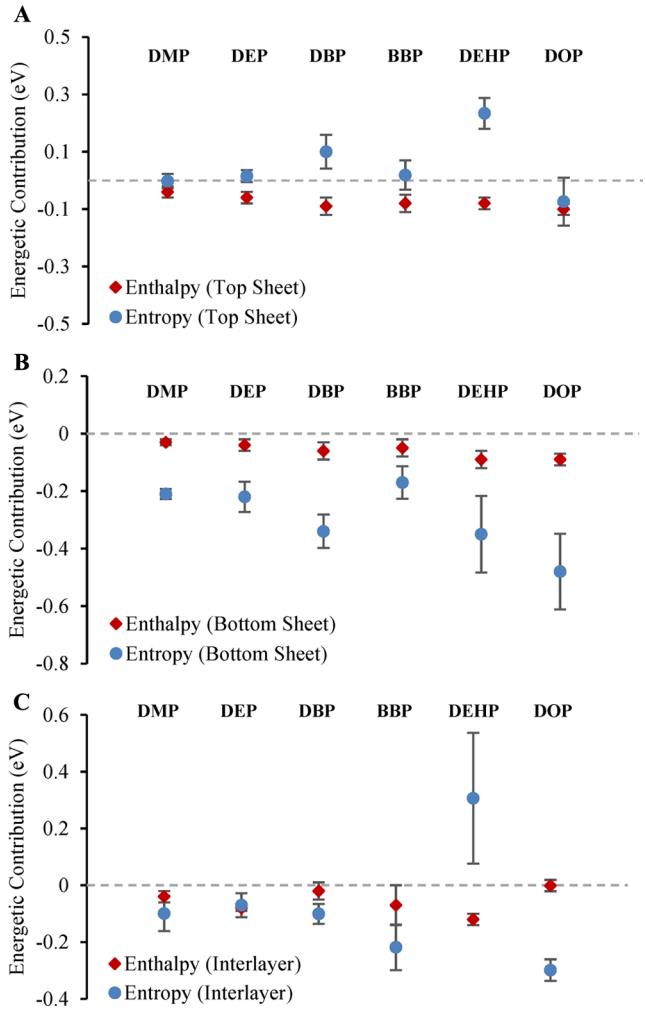

Figure 6. Enthalpic (red diamonds) and entropic (blue circles) contributions to the free energy of adsorption for the upper (A), lower (B), and interlayer (C) regions. Error bars represent 95% CI. Full results are shown in Table S4.

Finally, the methodology developed and tested here in the case of phthalate esters can be readily adapted to examine

DOI: 10.1021/acs.jpcc.9b01864
J. Phys. Chem. C 2019, 123, 13624−13636

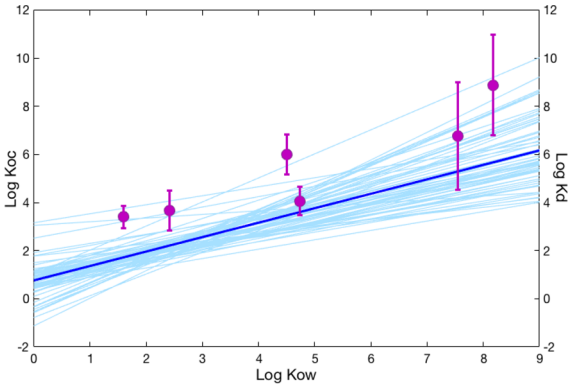

Figure 7. Compilation of reported log K_{ow}–log K_{oc} linear relationships for organic contaminants (light blue lines) and their average (dark blue line with a slope of 0.60 and an intercept of 0.76).[13,14,113−129] Phthalate log K_d values from this work are plotted as purple circles. Error bars represent 95% CI.

other uncharged organic contaminants as well as cationic, anionic, and zwitterionic compounds in addition to toxic and unstable compounds that are not easily studied in a wet-lab setting. More broadly, it could provide insight into the adsorption of dissolved organic matter[133] or other molecules (e.g., DNA or other biomarkers),[134] into the interplay between different organic compounds on clay surfaces, and into the affinity of dissolved organic molecules for other solid phases including soil organic matter and synthetic adsorbents.

■ ASSOCIATED CONTENT

Supporting Information

The Supporting Information is available free of charge on the ACS Publications website at DOI: 10.1021/acs.jpcc.9b01864.

Compiled literature data for DMP partitioning in soils; molecular dynamics simulations parameters and interatomic potentials; batch adsorption experimental methodology and isotherms; XRD data; simulation water and calcium density profiles; numerical results for simulation free energies, enthalpies, and entropies (PDF)

■ AUTHOR INFORMATION

Corresponding Author

*E-mail: jarw@princeton.edu.

ORCID

Jennifer A. R. Willemsen: 0000-0002-4018-6466

Ian C. Bourg: 0000-0002-5265-7229

Notes

The authors declare no competing financial interest.

■ ACKNOWLEDGMENTS

This research was supported equally by the U.S. Department of Energy, Office of Science, Office of Basic Energy Sciences, Geosciences Program under Award DE-SC0018419 and by the Princeton Environmental Institute through its Grand Challenges Program and Carbon Mitigation Initiative at Princeton University. Molecular dynamics simulations were performed using resources of the National Energy Research Scientific Computing Center (NERSC), which is supported by the U.S. Department of Energy, Office of Sciences, under Award DE-AC02-05CH11231.

■ REFERENCES

(1) Petrie, B.; Barden, R.; Kasprzyk-Hordern, B. A Review on Emerging Contaminants in Wastewaters and the Environment: Current Knowledge, Understudied Areas and Recommendations for Future Monitoring. *Water Res.* **2015**, *72*, 3−27.

(2) Luo, Y.; Guo, W.; Ngo, H. H.; Nghiem, L. D.; Hai, F. I.; Zhang, J.; Liang, S.; Wang, X. C. A Review on the Occurrence of Micropollutants in the Aquatic Environment and their Fate and Removal During Wastewater Treatment. *Sci. Total Environ.* **2014**, *473−474*, 619−641.

(3) Attina, T. M.; Hauser, R.; Sathyanarayana, S.; Hunt, P. A.; Bourguignon, J. P.; Myers, J. P.; DiGangi, J.; Zoeller, R. T.; Trasande, L. Exposure to Endocrine-Disrupting Chemicals in the USA: a Population-Based Disease Burden and Cost Analysis. *Lancet Diabetes Endocrinol.* **2016**, *4*, 996−1003.

(4) Ritter, S. The Human Cost of Chemical Exposure. *Chem. Eng. News* **2016**, *94*, 5−5.

(5) Trasande, L.; Zoeller, R. T.; Hass, U.; Kortenkamp, A.; Grandjean, P.; Myers, J. P.; DiGangi, J.; Hunt, P. M.; Rudel, R.; Sathyanarayana, S.; et al. Burden of Disease and Costs of Exposure to Endocrine Disrupting Chemicals in the European Union: An Updated Analysis. *Andrology* **2016**, *4*, 565−572.

(6) Weber, W. J., Jr.; McGinley, P. M.; Katz, L. E. Sorption Phenomena in Subsurface Systems: Concepts, Models and Effects on Contaminant Fate and Transport. *Water Res.* **1991**, *25*, 499−528.

(7) Schwarzenbach, R. P.; Escher, B. I.; Fenner, K.; Hofsetter, T. B.; Johnson, C. A.; von Gunten, U.; Wehrli, B. The Challenge of Micropollutants in Aquatic Systems. *Science* **2006**, *313*, 1072−1077.

(8) Jury, W. A.; Spencer, W. F.; Farmer, W. J. Behavior Assessment Model for Trace Organics in Soil: 1. Model Description. *J. Environ. Qual.* **1983**, *12*, 558−564.

(9) Brusseau, M. L.; Rao, P. S. C.; Gillham, R. W. Sorption Nonideality During Organic Contaminant Transport in Porous Media. *Crit. Rev. Environ. Control* **1989**, *19*, 33−99.

(10) Karickhoff, S. W.; Brown, D. S.; Scott, T. A. Sorption of Hydrophobic Pollutants on Natural Sediments. *Water Res.* **1979**, *13*, 241−248.

(11) Chiou, C. T.; Peters, L. J.; Freed, V. H. A Physical Concept of Soil-Water Equilibria for Nonionic Organic Compounds. *Science* **1979**, *206*, 831−832.

(12) Means, J. C.; Wood, S. G.; Hassett, J. J.; Banwart, W. L. Sorption of Polynuclear Aromatic Hydrocarbons by Sediments and Soils. *Environ. Sci. Technol.* **1980**, *14*, 1524−1528.

(13) Karickhoff, S. W. Semi-Empirical Estimation of Sorption of Hydrophobic Pollutants on Natural Sediments and Soils. *Chemosphere* **1981**, *10*, 833−846.

(14) Means, J. C.; Wood, S. G.; Hassett, J. J.; Banwart, W. L. Sorption of Amino-and Carboxy-Substituted Polynuclear Aromatic Hydrocarbons by Sediments and Soils. *Environ. Sci. Technol.* **1982**, *16*, 93−98.

(15) Hassett, J. J.; Banwart, W. L.; Wood, S. G.; Means, J. C. Sorption of α-Naphthol: Implications Concerning the Limits of Hydrophobic Sorption. *Soil Sci. Soc. Am. J.* **1981**, *45*, 38−42.

(16) Mingelgrin, U.; Gerstl, Z. Reevaluation of Partitioning as a Mechanism of Nonionic Chemicals Adsorption in Soils. *J. Environ. Qual.* **1983**, *12*, 1−11.

(17) Karickhoff, S. W. Organic Pollutant Sorption in Aquatic Systems. *J. Hydraul. Eng.* **1984**, *110*, 707−735.

(18) Grundl, T.; Small, G. Mineral Contributions to Atrazine and Alachlor Sorption in Soil Mixtures of Variable Organic Carbon and Clay Content. *J. Contam. Hydrol.* **1993**, *14*, 117−128.

(19) MacKay, A. A.; Vasudevan, D. Polyfunctional Ionogenic Compound Sorption: Challenges and New Approaches to Advance Predictive Models. *Environ. Sci. Technol.* **2012**, *46*, 9209−9223.

(20) Choi, Y. J.; Lee, L. S. Partitioning Behavior of Bisphenol Alternatives BPS and BPAF Compared to BPA. *Environ. Sci. Technol.* **2017**, *51*, 3725−3732.

(21) Sposito, G. *The Chemistry of Soils*; Oxford University Press: New York, 2016.

(22) Jaynes, W. F.; Boyd, S. A. Hydrophobicity of Siloxane Surfaces in Smectites as Revealed by Aromatic Hydrocarbon Adsorption from Water. *Clays Clay Miner.* **1991**, *39*, 428−436.
(23) Sposito, G.; Skipper, N. T.; Sutton, R.; Park, S.-h.; Soper, A. K.; Greathouse, J. A. Surface Geochemistry of the Clay Minerals. *Proc. Natl. Acad. Sci. U. S. A.* **1999**, *96*, 3358−3364.
(24) Aristilde, L.; Marichal, C.; Miéhé-Brendlé, J.; Lanson, B.; Charlet, L. Interactions of Oxytetracycline with a Smectite Clay: A Spectroscopic Study with Molecular Simulations. *Environ. Sci. Technol.* **2010**, *44*, 7839−7845.
(25) Weissmahr, K. W.; Haderlein, S. B.; Schwarzenbach, R. P. Complex Formation of Soil Minerals with Nitroaromatic Explosives and Other π-Acceptors. *Soil Sci. Soc. Am. J.* **1998**, *62*, 369−378.
(26) Sheng, G.; Johnston, C. T.; Teppen, B. J.; Boyd, S. A. Potential Contributions of Smectite Clays and Organic Matter to Pesticide Retention in Soils. *J. Agric. Food Chem.* **2001**, *49*, 2899−2907.
(27) Ransom, B.; Bennett, R. H.; Baerwald, R.; Shea, K. TEM Study of in Situ Organic Matter on Continental Margins: Occurrence and the "Monolayer" Hypothesis. *Mar. Geol.* **1997**, *138*, 1−9.
(28) Rasmussen, C.; Heckman, K.; Wieder, W. R.; Keiluweit, M.; Lawrence, C. R.; Berhe, A. A.; Blankinship, J. C.; Crow, S. E.; Druhan, J. L.; Hicks Pries, C. E.; et al. Beyond Clay: Towards an Improved Set of Variables for Predicting Soil Organic Matter Content. *Biogeochemistry* **2018**, *137*, 297−306.
(29) Keiluweit, M.; Kleber, M. Molecular-Level Interactions in Soils and Sediments: The Role of Aromatic π-Systems. *Environ. Sci. Technol.* **2009**, *43*, 3421−3429.
(30) Haderlein, S. B.; Weissmahr, K. W.; Schwarzenbach, R. P. Specific Adsorption of Nitroaromatic Explosives and Pesticides to Clay Minerals. *Environ. Sci. Technol.* **1996**, *30*, 612−622.
(31) Weissmahr, K. W.; Haderlein, S. B.; Schwarzenbach, R. P.; Hany, R.; Nüesch, R. In Situ Spectroscopic Investigations of Adsorption Mechanisms of Nitroaromatic Compounds at Clay Minerals. *Environ. Sci. Technol.* **1997**, *31*, 240−247.
(32) Zhu, D.; Herbert, B. E.; Schlautman, M. A.; Carraway, E. R.; Hur, J. Cation-π Bonding: A New Perspective on the Sorption of Polycyclic Aromatic Hydrocarbons to Mineral Surfaces. *J. Environ. Qual.* **2004**, *33*, 1322−1330.
(33) Zhu, D.; Herbert, B. E.; Schlautman, M. A.; Carraway, E. R. Characterization of Cation-π Interactions in Aqueous Solution using Deuterium nuclear magnetic resonance spectroscopy. *J. Environ. Qual.* **2004**, *33*, 276−284.
(34) Rana, K.; Boyd, S. A.; Teppen, B. J.; Li, H.; Liu, C.; Johnston, C. T. Probing the Microscopic Hydrophobicity of Smectite Surfaces. A Vibrational Spectroscopic Study of Dibenzo-*p*-dioxin Sorption to Smectite. *Phys. Chem. Chem. Phys.* **2009**, *11*, 2976−2985.
(35) Jeon, J.; Kannan, K.; Lim, B. J.; An, K. G.; Kim, S. D. Effects of Salinity and Organic Matter on the Partitioning of Perfluoroalkyl Acid (PFAs) to Clay Particles. *J. Environ. Monit.* **2011**, *13*, 1803−1810.
(36) Sposito, G.; Holtzclaw, K. M.; Charlet, L.; Jouany, C.; Page, A. L. Sodium-Calcium and Sodium-Magnesium Exchange on Wyoming Bentonite in Perchlorate and Chloride Background Ionic Media. *Soil Sci. Soc. Am. J.* **1983**, *47*, 51−56.
(37) Laird, D. A.; Shang, C. Relationship Between Cation Exchange Selectivity and Crystalline Swelling in Expanding 2:1 Phyllosilicates. *Clays Clay Miner.* **1997**, *45*, 681−689.
(38) Bourg, I. C.; Sposito, G. In *Handbook of Soil Sciences: Properties and Processes*; Huang, P. M., Li, Y., Sumner, M. E., Eds.; CRC Press: Boca Raton, FL, 2011; Chapter 16, pp 1−16.
(39) Boyd, S. A.; Sheng, G.; Teppen, B. J.; Johnston, C. T. Mechanisms for the Adsorption of Substituted Nitrobenzenes by Smectite Clays. *Environ. Sci. Technol.* **2001**, *35*, 4227−4234.
(40) Stackhouse, S.; Coveney, P. V.; Sandré, E. Plane-Wave Density Functional Theoretic Study of Formation of Clay-Polymer Nanocomposite Materials by Self-Catalyzed in Situ Intercalative Polymerization. *J. Am. Chem. Soc.* **2001**, *123*, 11764−11774.
(41) Sheng, G.; Johnston, C. T.; Teppen, B. J.; Boyd, S. A. Adsorption of Dinitrophenol Herbicides from Water by Montmorillonites. *Clays Clay Miner.* **2002**, *50*, 25−34.
(42) Chappell, M. A.; Laird, D. A.; Thompson, M. L.; Li, H.; Teppen, B. J.; Aggarwal, V.; Johnston, C. T.; Boyd, S. A. Influence of Smectite Hydration and Swelling on Atrazine Sorption Behavior. *Environ. Sci. Technol.* **2005**, *39*, 3150−3156.
(43) Gorb, L.; Lutchyn, R.; Zub, Y.; Leszczynska, D.; Leszczynski, J. The Origin of the Interaction of 1,3,5-Trinitrobenzene with Siloxane Surface of Clay Minerals. *J. Mol. Struct.: THEOCHEM* **2006**, *766*, 151−157.
(44) Aggarwal, V.; Chien, Y.-Y.; Teppen, B. J. Molecular Simulations to Estimate Thermodynamics for Adsorption of Polar Organic Solutes to Montmorillonite. *Eur. J. Soil Sci.* **2007**, *58*, 945−957.
(45) Liu, C.; Teppen, B. J.; Johnston, C. T.; Boyd, S. A. Mechanisms Associated with the High Adsorption of Dibenzo-p-Dioxin from Water by Smectite Clays. *Environ. Sci. Technol.* **2009**, *43*, 2777−2783.
(46) Aristilde, L.; Marichal, C.; Miéhé-Brendlé, J.; Lanson, B.; Charlet, L. Interactions of Oxytetracycline with a Smectite Clay: A Spectroscopic Study with Molecular Simulations. *Environ. Sci. Technol.* **2010**, *44*, 7839−7845.
(47) Zhu, R.; Chen, W.; Shapley, T. V.; Molinari, M.; Ge, F.; Parker, S. C. Sorptive Characteristics of Organomontmorillonite toward Organic Compounds: A Combined LFERs and Molecular Dynamics Simulation Study. *Environ. Sci. Technol.* **2011**, *45*, 6504−6510.
(48) Aristilde, L.; Lanson, B.; Miéhé-Brendlé, J.; Marichal, C.; Charlet, L. Enhanced Interlayer Trapping of a Tetracycline Antibiotic within Montmorillonite Layers in the Presence of Ca and Mg. *J. Colloid Interface Sci.* **2016**, *464*, 153−159.
(49) Okaikue-Woodi, F. E. K.; Kelch, S. E.; Schmidt, M. P.; Enid Martinez, C.; Youngman, R. E.; Aristilde, L. Structures and Mechanisms in Clay Nanopore Trapping of Structurally-Different Fluoroquinolone Antimicrobials. *J. Colloid Interface Sci.* **2018**, *513*, 367−378.
(50) Belzunces, B.; Hoyau, S.; Benoit, M.; Tarrat, N.; Bessac, F. Theoretical Study of the Atrazine Pesticide Interaction with Pyrophyllite and Ca^{2+} -Montmorillonite Clay Surfaces. *J. Comput. Chem.* **2017**, *38*, 133−143.
(51) Shapley, T. V.; Molinari, M.; Zhu, R.; Parker, S. C. Atomistic Modeling of the Sorption Free Energy of Dioxins at Clay-Water Interfaces. *J. Phys. Chem. C* **2013**, *117*, 24975−24984.
(52) Liu, C.; Gu, C.; Yu, K.; Li, H.; Teppen, B. J.; Johnston, C. T.; Boyd, S. A.; Zhou, D. Integrating Structural and Thermodynamics Mechanisms for Sorption of PCBs by Montmorillonite. *Environ. Sci. Technol.* **2015**, *49*, 2796−2805.
(53) Samaraweera, M.; Jolin, W.; Vasudevan, D.; MacKay, A. A.; Gascón, J. A. Atomistic Prediction of Sorption Free Energies of Caitonic Aromatic Amines on Montmorillonite: A Linear Interaction Energy Method. *Environ. Sci. Technol. Lett.* **2014**, *1*, 284−289.
(54) Laio, A.; Parrinello, M. Escaping Free-Energy Minima. *Proc. Natl. Acad. Sci. U. S. A.* **2002**, *99*, 12562−12566.
(55) Laio, A.; Gervasio, F. L. Metadynamics: A Method to Simulate Rare Events and Reconstruct the Free Energy in Biophysics, Chemistry and Material Science. *Rep. Prog. Phys.* **2008**, *71*, 126601.
(56) Ensing, B.; Laio, A.; Parrinello, M.; Klein, M. L. A Recipe for the Computation of the Free Energy Barrier and the Lowest Free Energy Path of Concerted Reactions. *J. Phys. Chem. B* **2005**, *109*, 6676−6687.
(57) Ensing, B.; De Vivo, M.; Liu, Z.; Moore, P.; Klein, M. L. Metadynamics as a Tool for Exploring Free Energy Landscapes of Chemical Reactions. *Acc. Chem. Res.* **2006**, *39*, 73−81.
(58) Lammers, L. N.; Bourg, I. C.; Okumura, M.; Kolluri, K.; Sposito, G.; Machida, M. Molecular Dynamics Simulations of Cesium Adsorption on Illite Nanoparticles. *J. Colloid Interface Sci.* **2017**, *490*, 608−620.
(59) Giam, C. S.; Chan, H. S.; Neff, G. S.; Atlas, E. L. Phthalates Ester Plasticzers: A New Class of Marine Pollutant. *Science* **1978**, *199*, 419−421.
(60) Yuan, S. Y.; Liu, C.; Liao, C. S.; Chang, B. V. Occurrence and Microbial Degradation of Phthalate Esters in Taiwain River Sediments. *Chemosphere* **2002**, *49*, 1295−1299.

DOI: 10.1021/acs.jpcc.9b01864
J. Phys. Chem. C 2019, 123, 13624−13636

(61) Fromme, H.; Küchler, T.; Otto, T.; Pilz, K.; Müller, J.; Wenzel, A. Occurrence of Phthalates and Bisphenol A and F in the Environment. *Water Res.* **2002**, *36*, 1429−1438.
(62) Sha, Y.; Xia, X.; Yang, Z.; Huang, G. H. Distribution of PAEs in the Middle and Lower Reaches of the Yellow River, China. *Environ. Monit. Assess.* **2007**, *124*, 277−287.
(63) U.S. Department of Health and Human Services: Centers for Disease Control and Prevention. Fourth National Report on Human Exposure to Environmental Chemicals: Updated Tables, March 2018, Volume One, 2018.
(64) Gray, T. J. B.; Butterworth, K. R.; Gaunt, I. F.; Grasso, P.; Gangolli, S. D. Short-Term Toxicity Study of Di(2- Ethylhexyl) Phthalate in Rats. *Food Cosmet. Toxicol.* **1977**, *15*, 389−399.
(65) Jarfelt, K.; Dalgaard, M.; Hass, U.; Borch, J.; Jacobsen, H.; Ladefoged, O. Antiandrogenic Effects in Male Rats Perinatally Exposed to a Mixture of Di(2-Ethylhexyl) Phthalate and Di(2-Ethylhexyl) Adipate. *Reprod. Toxicol.* **2005**, *19*, 505−515.
(66) Tyl, R. W.; Price, C. J.; Marr, M. C.; Kimmel, C. A. Developmental Toxicity Evaluation of Dietary Di(2-Ethylhexyl) Phthalate in Fischer 344 Rats and CD-1 Mice. *Toxicol. Sci.* **1988**, *10*, 395−412.
(67) Nikonorow, M.; Mazur, H.; Piekacz, H. Effect of Orally Administered Plasticizers and Polyvinyl Chloride Stabilizers in the Rat. *Toxicol. Appl. Pharmacol.* **1973**, *26*, 253−259.
(68) Zhao, X.-K.; Yang, G.-P.; Wang, Y.-J. Adsorption of Dimethyl Phthalate on Marine Sediments. *Water, Air, Soil Pollut.* **2004**, *157*, 179−192.
(69) Yang, F.; Wang, M.; Wang, Z. Sorption Behavior of 17 Phthalic Acid Esters on Three Soils: Effects of pH and Dissolved Organic Matter, Sorption Coefficient Measurement and QSPR Study. *Chemosphere* **2013**, *93*, 82−89.
(70) Liu, H.; Zhang, D.; Li, M.; Tong, L.; Feng, L. Competitive Adsorption and Transport of Phthalate Esters in the Clay Layer of JiangHan Plain, China. *Chemosphere* **2013**, *92*, 1542−1549.
(71) Banerjee, P.; Piwoni, M. D.; Ebeid, K. Sorption of Organic Contaminants to a Low Carbon Subsurface Core. *Chemosphere* **1985**, *14*, 1057−1067.
(72) Li, B.; Qian, Y.; Bi, E.; Chen, H.; Schmidt, T. C. Sorption Behavior of Phthalic Acid Esters on Reference Soils Evaluated by Soil Column Chromatography. *Clean: Soil, Air, Water* **2010**, *38*, 425−429.
(73) Hunter, J. G.; Uchrin, C. G. Adsorption of Phthalate Esters on Soil at Near Saturation Conditions. *J. Environ. Sci. Health, Part A: Toxic/Hazard. Subst. Environ. Eng.* **2000**, *A35*, 1503−1515.
(74) Maraqa, M. A. Effects of Fundamental Differences Between Batch and Miscible Displacement Techniques on Sorption Distribution Coefficient. *Environ. Geol.* **2001**, *41*, 219−228.
(75) Howard, P. H.; Banerjee, S.; Robillard, K. H. Measurement of Water Solubilities, Octanol/Water Partition Coefficients and Vapor Pressures of Commercial Phthalate Esters. *Environ. Toxicol. Chem.* **1985**, *4*, 653−661.
(76) Tsipursky, S. I.; Drits, V. A. The Distribution of Octahedral Cations in the 2:1 Layers of Dioctahedral Smectites Studied by Oblique-Texture Electron Diffraction. *Clay Miner.* **1984**, *19*, 177−193.
(77) Norman White, G.; Zelazny, L. W. Analysis and Implications of the Edge Structure of Dioctahedral Phyllosilicates. *Clays Clay Miner.* **1988**, *36*, 141−146.
(78) Tournassat, C.; Bourg, I. C.; Holmboe, M.; Sposito, G.; Steefel, C. I. Molecular Dynamics Simulations of Anion Exclusion in Clay Interlayer Nanopores. *Clays Clay Miner.* **2016**, *64*, 374−388.
(79) Morodome, S.; Kawamura, K. Swelling Behavior of Na- and Ca-Montmorillonite up to 150°C by *in Situ* X-ray Diffraction Experiments. *Clays Clay Miner.* **2009**, *57*, 150−160.
(80) Teich-McGoldrick, S. L.; Greathouse, J. A.; Jové-Colón, C. F.; Cygan, R. T. Swelling Properties of Montmorillonite and Beidellite Clay Minerals from Molecular Simulation: Comparison of Temperature, Interlayer Cation, and Charge Location Effects. *J. Phys. Chem. C* **2015**, *119*, 20880−20891.
(81) Cygan, R. T.; Liang, J.-J.; Kalinichev, A. G. Molecular Models of Hydroxide, Oxyhydroxide, and Clay Phases and the Development of a General Force Field. *J. Phys. Chem. B* **2004**, *108*, 1255−1266.
(82) Jorgensen, W. L.; Maxwell, D. S.; Tirado-Rives, J. Development and Testing of the OPLS All-Atom Force Field on Conformational Energetics and Properties of Organic Liquids. *J. Am. Chem. Soc.* **1996**, *118*, 11225−11236.
(83) Berendsen, H. J. C.; Grigera, J. R.; Straatsma, T. P. The Missing Term in Effective Pair Potentials. *J. Phys. Chem.* **1987**, *91*, 6269−6271.
(84) Åqvist, J. Ion-Water Interaction Potentials Derived from Free Energy Perturbation Simulations. *J. Phys. Chem.* **1990**, *94*, 8021−8024.
(85) Smith, D. E.; Dang, L. X. Computer Simulations of NaCl Association in Polarizable Water. *J. Chem. Phys.* **1994**, *100*, 3757−3766.
(86) Wasserman, E.; Wood, B.; Brodhol, J. The Static Dielectric Constant of Water at Pressures up to 20 kbar and Temperatures to 1273 K: Experiment, Simulations, and Empirical Equations. *Geochim. Cosmochim. Acta* **1995**, *59*, 1−6.
(87) Hura, G.; Russo, D.; Glaeser, R. M.; Head-Gordon, T.; Krack, M.; Parrinello, M. Water Structure as a Function of Temperature from X-Ray Scattering Experiments and Ab Initio Molecular Dynamics. *Phys. Chem. Chem. Phys.* **2003**, *5*, 1981−1991.
(88) Bourg, I. C.; Sposito, G. Connecting the Molecular Scale to the Continuum Scale for Diffusion Processes in Smectite-Rich Porous Media. *Environ. Sci. Technol.* **2010**, *44*, 2085−2091.
(89) Holmboe, M.; Bourg, I. C. Molecular Dynamics Simulations of Water and Sodium Diffusion in Smectite Interlayer Nanopores as a Function of Pore Size and Temperature. *J. Phys. Chem. C* **2014**, *118*, 1001−1013.
(90) Bourg, I. C.; Lee, S. S.; Fenter, P.; Tournassat, C. Stern Layer Structure and Energetics at Mica-Water Interfaces. *J. Phys. Chem. C* **2017**, *121*, 9402−9412.
(91) Cygan, R. T.; Guggenheim, S.; Koster van Groos, A. F. Molecular Models for the Intercalation of Methane Hydrate Complexes in Montmorillonite Clay. *J. Phys. Chem. B* **2004**, *108*, 15141−15149.
(92) Liu, X.; Lu, X.; Wang, R.; Zhou, H.; Xu, S. Interlayer Structure and Dynamics of Alkylammonium-Intercalated Smectites with and without Water: A Molecular Dynamics Study. *Clays Clay Miner.* **2007**, *55*, 554−564.
(93) Newton, A. G.; Sposito, G. Molecular Dynamics Simulations of Pyrophyllite Edge Surfaces: Structure, Surface Energies, and Solvent Accessibility. *Clays Clay Miner.* **2015**, *63*, 277−289.
(94) Ebrahimi, D.; Whittle, A. J.; Pellenq, R. J.-M. Mesoscale Properties of Clay Aggregates from Potential of Mean Force Representation of Interactions Between Nanoplatelets. *J. Chem. Phys.* **2014**, *140*, 154309.
(95) Plimpton, S. Fast Parallel Algorithms for Short-Range Molecular Dynamics. *J. Comput. Phys.* **1995**, *117*, 1−19.
(96) Fiorin, G.; Klein, M. L.; Hénin, J. Using Collective Variables to Drive Molecular Dynamics Simulations. *Mol. Phys.* **2013**, *111*, 3345−3362.
(97) Eastwood, J. W.; Hockney, R. W.; Lawrence, D. N. P3M3DP − The Three-Dimensional Periodic Particle-Particle/Particle-Mesh Program. *Comput. Phys. Commun.* **1980**, *19*, 215−261.
(98) Ryckaert, J.-P.; Ciccotti, G.; Berendsen, J. C. H. Numerical Integration of the Cartesian Equations of Motion of a System with Constraints: Molecular Dynamics of *N*-Alkanes. *J. Comput. Phys.* **1977**, *23*, 327−341.
(99) Humphrey, W.; Dalke, A.; Schulten, K. VMD: Visual Molecular Dynamics. *J. Mol. Graphics* **1996**, *14*, 33−38.
(100) Sposito, G. *The Sufrace Chemistry of Natural Particles*; Oxford University Press: New York, 2004.
(101) Arroyo, L. J.; Li, H.; Teppen, B. J.; Boyd, S. A. A Simple Method for Partial Purification of Reference Clays. *Clays Clay Miner.* **2005**, *53*, 511−520.

DOI: 10.1021/acs.jpcc.9b01864
J. Phys. Chem. C 2019, 123, 13624−13636

(102) Tinnacher, R. M.; Holmboe, M.; Tournassat, C.; Bourg, I. C.; Davis, J. A. Ion Adsorption and Diffusion in Smectite: Molecular, Pore, and Continuum Scale Views. *Geochim. Cosmochim. Acta* **2016**, *177*, 130−149.
(103) Ferrage, E.; Lanson, B.; Malikova, N.; Plançon, A.; Sakharov, B. A.; Drits, V. A. New Insights on the Distribution of Interlayer Water in Bi-Hydrated Smectite from X-ray Diffraction Profile Modeling of 00*l* Reflections. *Chem. Mater.* **2005**, *17*, 3499−3512.
(104) Wu, Y.; Si, Y.; Zhou, D.; Gao, J. Adsorption of Diethyl Phthalate Ester to Clay Minerals. *Chemosphere* **2015**, *119*, 690−696.
(105) Laird, D. A.; Barriuso, E.; Dowdy, R. H.; Koskinen, W. C. Adsorption of Atrazine on Smectites. *Soil. Sci. Soc. Am. J.* **1992**, *56*, 62−67.
(106) The Clay Minerals Society. Physical and Chemical Data of Source Clays; http://www.clays.org/sourceclays_data.html (accessed Dec 12, 2018).
(107) Bourg, I. C.; Sposito, G.; Bourg, A. C. M. Modeling the Acid-Base Surface Chemistry of Motmorillonite. *J. Colloid Interface Sci.* **2007**, *312*, 297−310.
(108) Tournassat, C.; Greneche, J. M.; Tisserand, D.; Charlet, L. The Titration of Clay Minerals I. Discontinuous Backtitration Technique Combined with CEC Measurements. *J. Colloid Interface Sci.* **2004**, *273*, 224−233.
(109) Anderson, S. J.; Sposito, G. Cesium-Adorption Method for Measuring Accessible Structural Surface Charge. *Soil Sci. Soc. Am. J.* **1991**, *55*, 1569−1576.
(110) Duc, M.; Gaboriaud, F.; Thomas, F. Sensitivity of the Acid-Base Properties of Clays to the Methods of Preparation and Measurement 2. Evidence from Continuous Potentiometric Titrations. *J. Colloid Interface Sci.* **2005**, *289*, 148−156.
(111) Chen, F.; Smith, P. E. Simulated Surface Tensions of Common Water Models. *J. Chem. Phys.* **2007**, *126*, 221101.
(112) Teppen, B. J.; Aggarwal, V. Thermodynamcis of Organic Cation Exchange Selectivity in Smectites. *Clays Clay Miner.* **2007**, *55*, 119−130.
(113) Gawlik, B. M.; Sotiriou, N.; Feicht, E. A.; Schulte-Hostede, S.; Kettrup, A. Alternatives for the Determination of the Soil Adsorption Coefficient, Koc, of Non-Ionic Organic Compounds − A Review. *Chemosphere* **1997**, *34*, 2525−2551.
(114) Briggs, G. G. Theoretical and Experimental Relationships Between Soil Adsorption, Octanol-Water Partition Coefficients, Water Solubilities, Bioconcentration Factors, and the Parachor. *J. Agric. Food Chem.* **1981**, *29*, 1050−1059.
(115) Kanazawa, J. Relationship Between the Soil Sorption Constants for Pesticides and their Physicochemical Properties. *Environ. Toxicol. Chem.* **1989**, *8*, 477−484.
(116) Gerstl, Z. Estimation of Organic Chemical Sorption by Soils. *J. Contam. Hydrol.* **1990**, *6*, 357−375.
(117) Chin, Y.-P.; Peven, C. S.; Weber, W. J., Jr. Estimating Soil/Sediment Partition Coefficients for Organic Compounds by High Performance Reverse Phase Liquid Chromatography. *Water Res.* **1988**, *22*, 873−881.
(118) Vowles, P. D.; Mantoura, R. F. C. Sediment-Water Partition Coefficients and HPLC-Retention Factors of Aromatic Hydrocarbons. *Chemosphere* **1987**, *16*, 109−116.
(119) Chiou, C. T.; Porter, P. E.; Schmedding, D. W. Partition Equilibria of Non-Ionic Organic Compounds Between Soil Organic Matter and Water. *Environ. Sci. Technol.* **1983**, *17*, 227−231.
(120) Gerstl, Z.; Mingelgrin, U. Sorption of Organic Substances by Soils and Sediments. *J. Environ. Sci. Health, Part B* **1984**, *19*, 297−312.
(121) Müller, M.; Kördel, W. Comparison of Screening Methods for the Estimation of Adsorption Coefficients on Soil. *Chemosphere* **1996**, *32*, 2493−2504.
(122) Sabljić, A.; Güsten, H.; Verhaar, H.; Hermens, J. QSAR Modelling of Soil Sorption. Improvements and Systematics of Log K_{oc} Versus Log K_{ow} Correlations. *Chemosphere* **1995**, *31*, 4489−4514.
(123) Noegrohati, S.; Hammers, W. E. Regression Models for some Solute Distribution Equilibria in the Terrestrial Environment. *Toxicol. Environ. Chem.* **1992**, *34*, 175−195.
(124) Szabó, G.; Prosser, S. L.; Bulman, R. A. Determination of the Adsorption Coefficient (K_{oc}) of some Aromatics for Soil by RP-HPLC on Two Immobilized Humic Acid Phases. *Chemosphere* **1990**, *21*, 777−778.
(125) van Gestel, C. A. M.; Ma, W.-c.; Smit, C. E. Development of QSARs in Terrestrial Ecotoxicology: Earthworm Toxicity and Soil Sorption of Chlorophenols, Chlorobenzenes and Dichloroaniline. *Sci. Total Environ.* **1991**, *109-110*, 589−604.
(126) Szabó, G.; Guczi, J.; Bulman, R. A. Examination of Silica-Salicylic Acid and Silica-8-Hydroxyquinoline HPLC Stationary Phases for the Estimation of the Adsorption Coefficient of Soil for some Aromatic Hydrocarbons. *Chemosphere* **1995**, *30*, 1717−1727.
(127) Hodson, J.; Williams, N. A. The Estimation of the Adsorption Coefficient (K_{oc}) for Soils by High Performance Liquid Chromatography. *Chemosphere* **1988**, *17*, 67−77.
(128) Pussemier, L.; Szabó, G.; Bulman, R. A. Prediction of the Soil Adsorption Coefficient K_{oc} for Aromatic Pollutants. *Chemosphere* **1990**, *21*, 1199−1212.
(129) Schwarzenbach, R. P.; Westall, J. Transport of Nonpolar Organic Compounds from Surface Water to Groundwater. Laboratory Sorption Studies. *Environ. Sci. Technol.* **1981**, *15*, 1360−1367.
(130) Coward, E. K.; Ohno, T.; Plante, A. F. Adsorption and Molecular Fractionation of Dissolved Organic Matter on Iron-Bearing Mineral Matrices of Varying Crystallinity. *Environ. Sci. Technol.* **2018**, *52*, 1036−1044.
(131) Chassé, A. W.; Ohno, T.; Higgins, S. R.; Amirbahman, A.; Yildirim, N.; Parr, T. B. Chemical Force Spectroscopy Evidence Supporting the Layer-by-Layer Model of Organic Matter Binding to Iron (oxy)Hydroxide Mineral Surfaces. *Environ. Sci. Technol.* **2015**, *49*, 9733−9741.
(132) Lehmann, J.; Kleber, M. The Contentious Nature of Soil Organic Matter. *Nature* **2015**, *528*, 60−68.
(133) Kleber, M.; Sollins, P.; Sutton, R. A Conceptual Model of Organo-Mineral Interactions in Soils: Self-Assembly of Organic Molecular Fragments into Zonal Structures on Mineral Surfaces. *Biogeochemistry* **2007**, *85*, 9−24.
(134) Thyveetil, M.-A.; Coveney, P. V.; Greenwell, H. C.; Suter, J. L. Computer Simulation Study of the Structural Stability and Materials Properties of DNA-Intercalated Layered Double Hydroxides. *J. Am. Chem. Soc.* **2008**, *130*, 4742−4756.

DOI: 10.1021/acs.jpcc.9b01864
J. Phys. Chem. C 2019, 123, 13624−13636